Lasing in robust cesium lead halide perovskite nanowires

Samuel W. Eaton[a], Minliang Lai[a], Natalie A. Gibson[a,b], Andrew B. Wong[a,c], Letian Dou[a,c], Jie Ma[c,d], Lin-Wang Wang[c,d], Stephen R. Leone[a,b,e,1], and Peidong Yang[a,c,f,1]

[a]Department of Chemistry, University of California, Berkeley, CA 94720; [b]Chemical Sciences Division, Lawrence Berkeley National Laboratory, Berkeley, CA 94720; [c]Materials Sciences Division, Lawrence Berkeley National Laboratory, Berkeley, CA 94720; [d]Joint Center for Artificial Photosynthesis, Lawrence Berkeley National Laboratory, Berkeley, CA 94720; [e]Department of Physics, University of California, Berkeley, CA 94720; and [f]Kavli Energy NanoSciences Institute, Berkeley, CA 94720

Contributed by Stephen R. Leone, January 19, 2016 (sent for review January 13, 2016; reviewed by Xiangfeng Duan and Edward H. Sargent)

The rapidly growing field of nanoscale lasers can be advanced through the discovery of new, tunable light sources. The emission wavelength tunability demonstrated in perovskite materials is an attractive property for nanoscale lasers. Whereas organic–inorganic lead halide perovskite materials are known for their instability, cesium lead halides offer a robust alternative without sacrificing emission tunability or ease of synthesis. Here, we report the low-temperature, solution-phase growth of cesium lead halide nanowires exhibiting low-threshold lasing and high stability. The as-grown nanowires are single crystalline with well-formed facets, and act as high-quality laser cavities. The nanowires display excellent stability while stored and handled under ambient conditions over the course of weeks. Upon optical excitation, Fabry–Pérot lasing occurs in $CsPbBr_3$ nanowires with an onset of 5 μJ cm^{-2} with the nanowire cavity displaying a maximum quality factor of 1,009 ± 5. Lasing under constant, pulsed excitation can be maintained for over 1 h, the equivalent of 10^9 excitation cycles, and lasing persists upon exposure to ambient atmosphere. Wavelength tunability in the green and blue regions of the spectrum in conjunction with excellent stability makes these nanowire lasers attractive for device fabrication.

nanowire | perovskite | laser | inorganic | stability

Miniaturized light sources hold great promise for advancing the field of optoelectronics. The development of highly stable, wavelength-tunable light sources on the nanoscale can unlock the potential for commercial applications in optical communications (1, 2), sensing (3), imaging (4), and data storage (5), among many others. Nanowire lasers represent one promising approach toward miniaturized light sources. Acting both as the laser cavity and gain medium (6), nanowires may be easily incorporated into optoelectronic circuits based on their size as well as recent advances in electrical pumping (7–10). A wide range of nanowire lasers has been reported consisting of a multitude of compositions including many II–VI and III–V semiconductors (11). Unfortunately, fabrication of many of these nanowires requires expensive high-temperature or low-pressure conditions. Additionally, whereas most are stable under ambient conditions, only a few of these materials have demonstrated broad wavelength tunability. The recent discovery of the favorable properties of methyl ammonium lead halide perovskite materials has triggered a paradigm shift in what is possible in optoelectronics. Stoichiometric wavelength tunability, low trap state density, solution-phase processability, as well as excellent light absorption and emission, make these materials well suited to applications in solar cells (12–15), light-emitting diodes (16, 17), photodetectors (18, 19), and lasers (20–22).

Recently, Zhu et al. reported low lasing thresholds and record-breaking quality factors for methyl ammonium lead halide ($CH_3NH_3PbX_3$, X = I, Br, Cl) nanowire lasers as well as excellent wavelength tunability achieved through halide substitution and alloying (20). However, these compositions are limited in their utility due to their intrinsic lack of stability due to autodegradation and susceptibility to hydrolysis from atmospheric water (23, 24). Multiple strategies have been pursued to improve the hybrid perovskite stability, including substituting or doping the methyl ammonium cation with less reactive cations such as formamide or inorganic atoms like cesium (25). An alternate approach is to abandon the organic cation altogether; for methyl ammonium lead bromide, full substitution of the organic methyl ammonium cation with cesium yields a perovskite-like structure, $CsPbBr_3$. With strikingly similar optical and electronic properties, cesium lead halide perovskites are favorable materials for laser gain media (26, 27). Whereas early studies revealed wide stoichiometric emission wavelength tunability (28), stimulated emission for all-inorganic perovskites was not reported until 2007 in thin films of $CsPbBr_3$ (29, 30). Recent reports have expanded the versatility of the cesium lead halides by demonstrating amplified spontaneous emission in a variety of $CsPbX_3$ compositions and alloys, as well as whispering gallery mode lasing in coated silica beads and microcrystals (31–33). Whereas these recent works have highlighted the impressive properties of cesium lead halide perovskites in terms of their optical properties and tunability, the growth and characterization of cesium lead halide nanowires capable of lasing has not yet been achieved. Here, we report a new method for the production of high-quality cesium lead bromide and cesium lead chloride nanowires as well as, to our knowledge, the first demonstration of lasing in all-inorganic perovskite nanowires. The low-temperature, solution-phase growth process affords well-faceted, crystalline nanowires with strong emissive properties and includes wavelength tunability over 100 nm via halide substitution. Pulsed optical excitation results in lasing at low thresholds and with quality factors comparable to previous nanowire laser reports. Most notably, the nanowires are stable for weeks under

Significance

Nanowire lasers are miniaturized light sources with great potential for integration into optoelectronic circuits. Many of the current nanowire lasers either require extreme conditions for synthesis or suffer from poor operational stability. We synthesize nanowires of a promising set of compositions, the cesium lead halides, and accomplish this under near-ambient conditions. These nanowires act as efficient laser cavities and are capable of lasing with relatively low excitation thresholds. They also demonstrate unprecedented stability for a perovskite-based nanowire laser and offer a new nanoscale platform for future study.

Author contributions: S.W.E., M.L., N.A.G., A.B.W., J.M., L.-W.W., S.R.L., and P.Y. designed research; S.W.E., M.L., N.A.G., A.B.W., L.D., and J.M. performed research; S.W.E., M.L., N.A.G., A.B.W., J.M., and P.Y. analyzed data; and S.W.E., M.L., N.A.G., S.R.L., and P.Y. wrote the paper.

Reviewers: X.D., University of California, Los Angeles; and E.H.S., University of Toronto.

The authors declare no conflict of interest.

[1]To whom correspondence may be addressed. Email: srl@berkeley.edu or p_yang@berkeley.edu.

This article contains supporting information online at www.pnas.org/lookup/suppl/doi:10.1073/pnas.1600789113/-/DCSupplemental.

ambient conditions and can be handled with little concern for degradation. This stability extends to lasing as well; cesium lead bromide nanowires are shown to lase for over 10^9 excitation cycles and continue to lase even when exposed to ambient atmosphere.

Results and Discussion

Our initial study focused on $CsPbBr_3$ nanowires, as previous reports suggest this composition is strongly photoluminescent (26, 34) and capable of stimulated emission (29–31). Although we have already reported the synthesis of colloidal $CsPbBr_3$ nanowires (34), those nanowires are too narrow (~20-nm diameter) to efficiently confine the 535-nm emission and are therefore unable to support photonic lasing (Fig. S1). To achieve lasing, nanowires with diameters greater than ~180 nm are required, but these are not currently accessible using the colloidal synthesis method. Alternatively, a low-temperature solution-phase process reported by Zhu et al. afforded single-crystal hybrid perovskite ($CH_3NH_3PbX_3$, X = Cl, Br, I) nanowires and nanoplates with diameters of a few hundred nanometers (20). Inspired by this method, we demonstrate a new solution growth process to synthesize single-crystal $CsPbX_3$ (X = Br, Cl) nanowires and nanoplates by dipping a PbI_2 thin film into a CsX–methanol solution with mild heating (50 °C). This method represents, to our knowledge, the first reported synthesis of surfactant-free $CsPbX_3$ nanowires and nanoplates through a simple, low-temperature, solution-phase process. A detailed discussion of the nanowire growth method may be found in the *Supporting Information* (Fig. S2). From the scanning electron microscopy (SEM) images shown in Fig. 1*A*, a wide range of $CsPbBr_3$ nanoscale morphologies was produced during the 12-h reaction including nanowires, nanocrystals, and nanoplates. The nanowires range in length from 2 to 40 μm and in width from 0.2 to 2.3 μm, placing them in an ideal size regime for photonic nanowire lasing. The majority of nanowires were found to have rectangular cross-sections (Fig. 1*A*, *Inset*) with strongly wire-dependent height-to-width ratios (Fig. S3). Nanowires were chosen for study based on the presence of clean, well-formed facets, which are critical for efficient emission confinement, and transferred by micromanipulator to a clean, fused silica substrate for all optical experiments (Fig. 1*B*).

The elemental composition and atomic structure of the nanowires were quantified to ensure they conformed to the expected, room-temperature orthorhombic phase of $CsPbBr_3$. The X-ray diffraction (XRD) pattern of the $CsPbBr_3$ growth substrate shows strong diffraction peaks which can be assigned to the pure orthorhombic crystal structure (space group Pbnm), and does not contain impurity peaks from either the PbI_2 or CsBr starting materials (Fig. 1*C*). The clear splitting of the narrow 002 and 110 peaks further indicates that the as-grown $CsPbBr_3$ is of the room-temperature orthorhombic phase and comprises large, crystalline domains. The nanowire composition was determined by energy-dispersive X-ray spectroscopy, which indicated the presence of Cs, Pb, and Br in a 1.1:1.0:2.7 ratio, in close agreement with the $CsPbBr_3$ phase (Fig. S4). The crystal structure of the nanowires was determined through selected area electron diffraction (SAED) as shown in Fig. 1*D*. The SAED pattern shown in Fig. 1*D* (*Inset*) indicates that the nanowires are single crystalline and may be indexed to the [110] zone axis of the orthorhombic phase of $CsPbBr_3$ in agreement with the XRD pattern. According to the SAED pattern, the nanowire growth direction was also indexed to the [002] direction of the orthorhombic phase of $CsPbBr_3$.

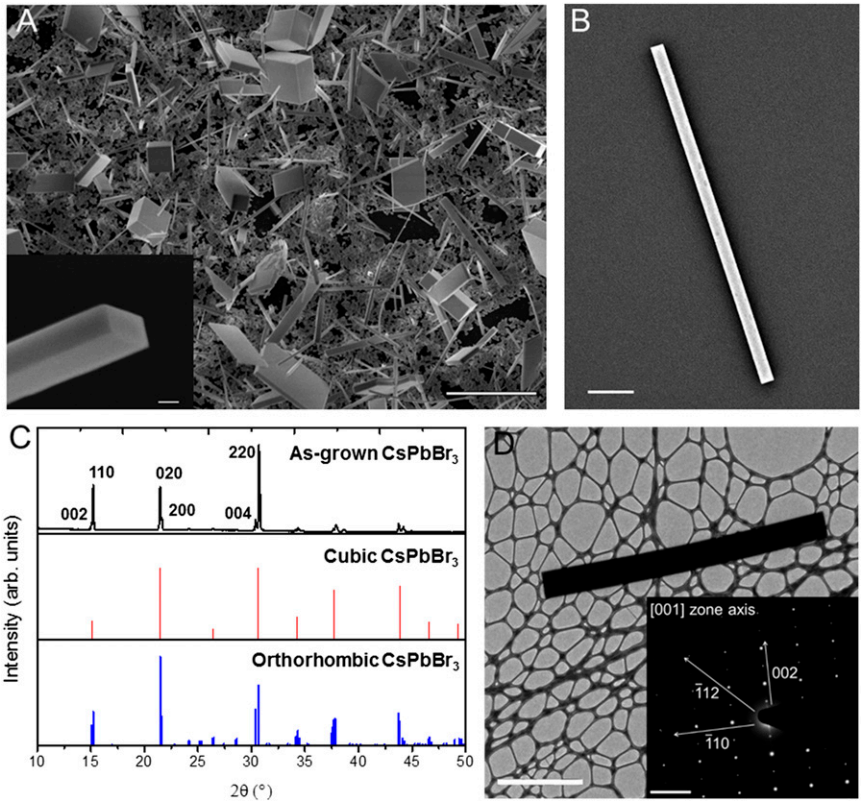

Fig. 1. Structural characterization of single-crystal $CsPbBr_3$ nanowires. (*A*) SEM images of $CsPbBr_3$ nanowires and nanoplates grown from PbI_2 in a methanolic solution of 8 mg/mL CsBr at 50 °C for 12 h. (Scale bar, 10 μm.) (*Inset*) SEM image of the rectangular end facet of a nanowire. (Scale bar, 500 nm.) (*B*) A single $CsPbBr_3$ nanowire isolated on a quartz substrate with a 5-nm Au sputter coat. (Scale bar, 1 μm.) (*C*) XRD pattern of as-grown $CsPbBr_3$ (black) with the standard XRD patterns of cubic (red) and orthorhombic (blue) $CsPbBr_3$. (*D*) TEM image of an individual nanowire. (Scale bar, 5 μm.) (*Inset*) SAED pattern from the same nanowire, with relevant crystallographic axes labeled. (Scale bar, 2 nm^{-1}.)

Photonic lasing arises from the unique ability of a nanowire to act as both gain medium and laser cavity. Forming the nanowire from a stable, highly absorptive, and emissive material allows for stimulated emission to occur upon reaching a sufficient carrier density (11, 35). The nanowire geometry defines the laser cavity, which is bounded on either end by the nanowire end facets. The difference in refractive index between the nanowire and its environment (atmosphere, substrate, etc.) generates significant end facet reflectivity as well as efficient wave guiding along the length of the wire. For $CsPbBr_3$ nanowires, lasing was achieved via optical excitation from a femtosecond pulsed laser. At excitation densities below the lasing threshold, spontaneous emission dominates, and the nanowire is uniformly emissive as shown in Fig. 2*B*. Upon surpassing the threshold, however, stimulated emission takes over and a periodic emission pattern is observed (Fig. 2 *C* and *D*), which is caused by interference of the coherent emission from the two end facets of the nanowire. The dependence of the photoluminescence (PL) spectral response on increasing excitation fluence is shown in Fig. 2*E*. The spontaneous emission from a $CsPbBr_3$ nanowire is centered at 516 nm with a 16-nm (74 meV) FWHM. The spontaneous emission peak first increases with increasing excitation intensity, then plateaus as narrow, closely spaced lasing peaks (0.5-nm minimum FWHM) emerge on the red edge of the emission spectrum near 532 nm and grow rapidly with excitation intensity. The narrow peaks correspond to Fabry–Pérot lasing modes as the mode spacing is found to change linearly with the inverse of the nanowire length (Fig. 2*F*, *Inset*). The power-dependent output

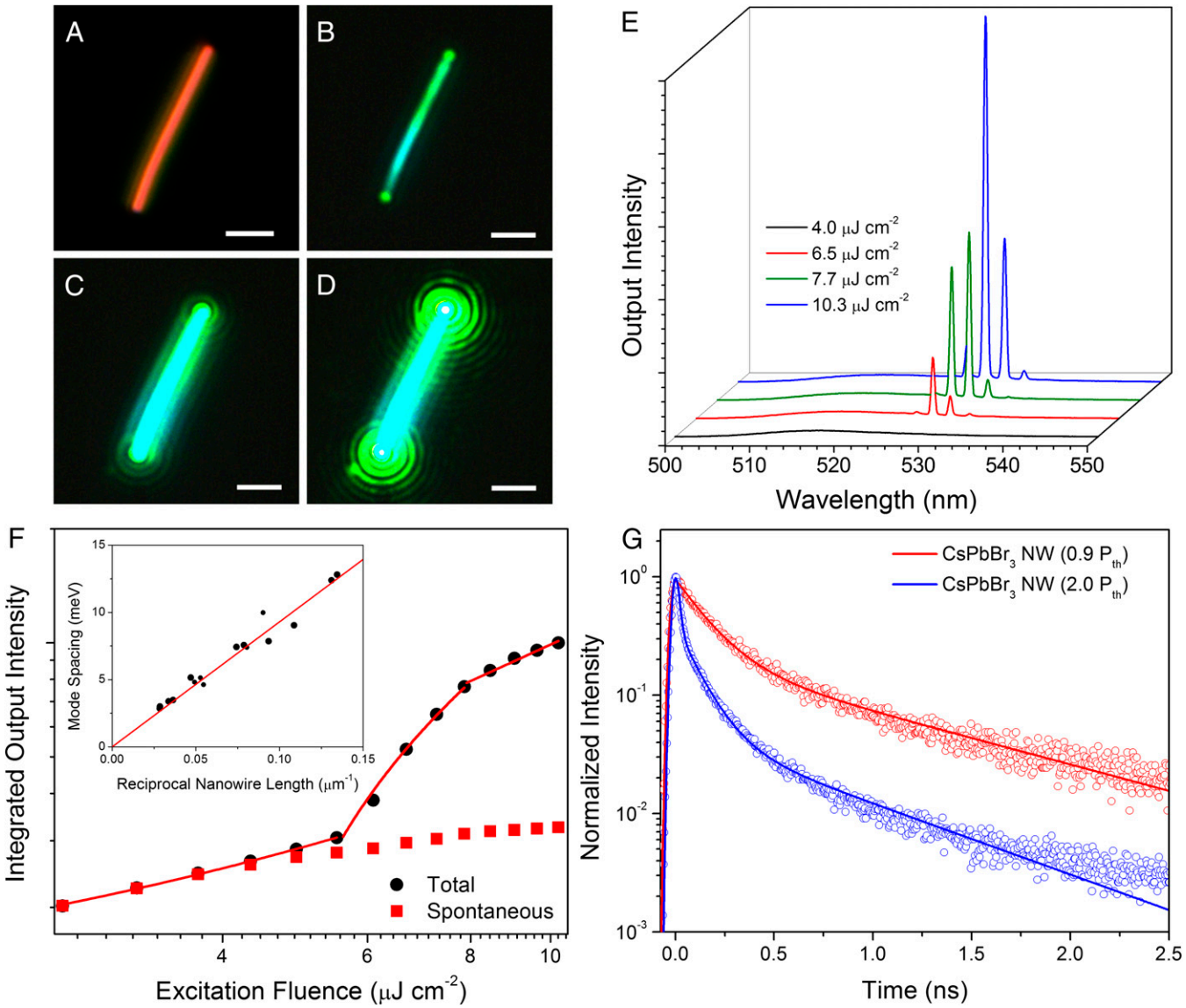

Fig. 2. Lasing in single-crystal $CsPbBr_3$ nanowires. (*A*) Dark-field image of a $CsPbBr_3$ nanowire. (*B–D*) The nanowire from *A* under excitation from a femtosecond pulsed laser with increasing excitation fluence. (Scale bar, 2 μm.) (*E*) Power-dependent emission spectra from the $CsPbBr_3$ nanowire shown in images *A–D*. Narrow emission peaks at ~530 nm are indicative of lasing. (*F*) The integrated output intensity of the $CsPbBr_3$ nanowire with increasing pump fluence (black circles) follows a typical S-curve pattern and can be linearly fit to show three separate emission regimes: spontaneous emission (<5 μJ cm^{-2}), amplified spontaneous emission (5–10 μJ cm^{-2}), and lasing (>10 μJ cm^{-2}). Spontaneous emission (red squares) from the nanowire plateaus as stimulated emission begins to dominate. (*Inset*) Plot of inverse nanowire length against mode spacing, confirming that Fabry–Pérot-type lasing is dominant. (*G*) TRPL from a $CsPbBr_3$ nanowire below (red) and above (blue) the lasing threshold (P_{th}). The emergence of a rapid decay component (<10 ps) suggests rapid carrier quenching due to stimulated emission.

intensity (Fig. 2*F*) follows the typical "S"-curve shape and depicts all three PL regimes: spontaneous emission dominates at low excitation intensities until the onset of lasing near 5 μJ cm^{-2} (P_{th}), the superlinear PL increase indicative of amplified spontaneous emission follows, and finally gain-pinning and the emergence of lasing occurs past 10 μJ cm^{-2} (36). The full set of power-dependent spectra is shown in Fig. S5*A*. Analysis of the individual peak widths from the spectra in Fig. 2*E* provides information about the nanowire laser cavity quality (Q) factor, or how well the cavity confines and amplifies emission. The Q factor is mode dependent with stronger modes possessing higher values because this corresponds to more efficient amplification and thus higher emission intensity. Using the relationship $Q = \lambda/\delta\lambda$, where λ is the peak center wavelength and δλ is the peak width, a maximum, single-mode Q factor of 1,009 ± 5 was determined with an average of 960 ± 60 when considering the four major modes (Fig. S6).

Time-resolved PL (TRPL) can be used to measure the carrier population dynamics of the laser cavity above and below the lasing threshold. Below the lasing threshold (Fig. 2*G*, red trace), the nanowire PL signal decays biexponentially with the rapid component (154 ± 2 ps, 81%) contributing much more than the slower component (970 ± 20 ps, 19%). Based on preliminary TRPL measurements of previously reported, surface-passivated, colloidal $CsPbX_3$ nanowires, which exhibit much longer lifetimes (>>1 ns), we attribute the rapid component to surface state recombination and the longer component to bulk recombination (34). When the excitation fluence is increased past the lasing threshold, an additional decay component is observed (<30 ps, 87%), which decays more rapidly than the other components (110 ± 2 ps, 11%; 720 ± 20 ps, 2%) as well as the instrument response. This rapid decay corresponds to the stimulated emission process depleting carriers that would otherwise undergo spontaneous emission. The low-lasing threshold and high-Q factor place these nanowires in the upper tier of nanowire lasers and clearly demonstrate the effectiveness of $CsPbBr_3$ as a gain medium (see refs. 10, 19, 31 for detailed lists of nanowire lasers and their performance characteristics).

The mechanism for optical gain by stimulated emission in perovskite nanostructures is still under investigation. In $CsPbX_3$ quantum dots, support for both single-exciton and biexciton lasing has been demonstrated (31, 33). In the case of biexciton-driven stimulated emission, a 50-meV red-shifted emission band was assigned to biexciton recombination, in agreement with expected biexciton binding energies in $CsPbX_3$ quantum dots (37). Whereas we observe a similar asymmetric red-shifted emission band at 290 and 6 K (Fig. S7), the red shift of 69 meV is an order of magnitude larger than expected for biexciton binding energies in non-quantum confined $CsPbBr_3$ nanowires. Instead, we postulate that an electron–hole plasma (EHP) mechanism is responsible for stimulated emission, as proposed in well-known compositions such as ZnO (38) and GaN (39) as well as in recent $CH_3NH_3PbX_3$ nanowires (20). An EHP is formed in bulk crystals when the carrier density surpasses the Mott density; here, the carrier density at the lasing threshold was estimated to be $\sim 6 \times 10^{17}$ cm^{-3} by finite-difference time-domain simulation (*Supporting Information*), a factor of 3 greater than the bulk $CsPbBr_3$ Mott density of $\sim 2 \times 10^{17}$ cm^{-3}. In addition, the formation of an EHP is expected to lead to a blue shift in the cavity modes due to a decrease in the refractive index that arises from exciton absorption saturation (38). We observe a blue shift of 2 nm with increasing excitation fluence (Fig. S5*B*), suggesting that an EHP mechanism is responsible for stimulated emission in $CsPbX_3$ nanowires. Further study is needed, however, to elucidate the stimulated emission carrier dynamics.

Cesium lead halide materials have been shown to be stable when exposed to atmospheric water or heat, making them attractive for real-world application (27, 33). The $CsPbBr_3$ nanowires reported here are stable for days under ambient atmosphere and illumination without loss of morphology. Additionally, the material composition remains intact over the course of months and does not separate into $PbBr_2$ and other byproducts as has been demonstrated for some hybrid perovskite materials (Fig. 3*A*) (24). $CsPbBr_3$ nanowires are also stable under constant, pulsed excitation above the lasing threshold. Nanowires were excited to 1.2 P_{th} under either a closed nitrogen atmosphere or ambient atmosphere (26 °C ± 0.5 °C, 50% ± 1% relative humidity) and the integrated emission intensity was monitored. The results shown in Fig. 3*B* indicate significant operating lifetimes even under atmospheric conditions. Under nitrogen, nanowire lasing continues uninterrupted for longer than 1 h or over 10^9 excitation cycles (Fig. 3*B*, blue trace), with the nanowire

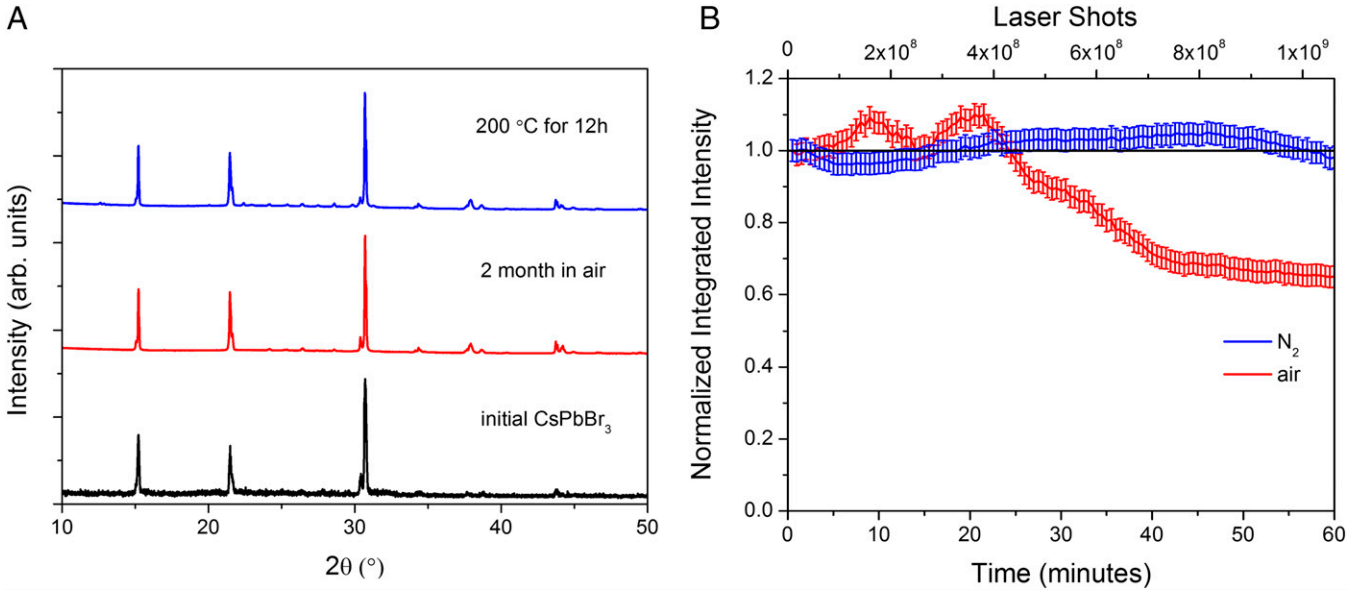

Fig. 3. Stability of $CsPbBr_3$. (*A*) XRD patterns of as-grown $CsPbBr_3$ before testing (black), after exposure to air for 2 mo (red), and after annealing at 200 °C (blue). In both cases, the $CsPbBr_3$ phase remained identical to the as-grown and indicated high compositional stability. (*B*) Integrated emission intensity for $CsPbBr_3$ nanowires under constant pulsed excitation (1.2 P_{th}) while exposed to nitrogen (blue) and ambient atmosphere (red).

undamaged after this time (Fig. S8). Under atmospheric conditions, lasing output is observed to decrease over the course of the experiment, but it does not fall below the original output until over 4.4×10^8 excitation cycles (Fig. 3*B*, red trace). In contrast, amplified spontaneous emission from thin films of $CsPbBr_3$ falls to 90% after only 1.6×10^7 excitation cycles (31). In hybrid perovskite materials, whispering gallery mode lasing in $CH_3NH_3PbI_3$ persists for 8×10^6 excitation cycles (40), whereas the long-term lasing stability of $CH_3NH_3PbX_3$ nanowires lasers has not been reported (20). The stable, continuous lasing operation observed here is promising for future applications as it suggests both high photo- and thermal stability under ideal or suboptimal environmental conditions.

Lasing is also possible for other $CsPbX_3$ compositions and geometries besides $CsPbBr_3$ nanowires. Single-crystal nanowires of $CsPbCl_3$ were successfully synthesized by replacing CsBr with CsCl during the reaction, with the XRD pattern confirming the expected tetragonal phase of the as-grown $CsPbCl_3$ (see Fig. S9 for characterization). The smooth, rectangular facets of the $CsPbCl_3$ nanowires, as well as the strong PL emission centered at 418 nm, make them ideal for extending the wavelength range of $CsPbX_3$ nanowire lasers. Upon focused excitation, lasing occurred near 430 nm with the emergence of narrow peaks similar to $CsPbBr_3$ nanowires as shown in Fig. 4*A*. The lasing threshold was found at ~86 μJ cm^{-2}, significantly higher than for $CsPbBr_3$ nanowires, and the Q factor was consequently found to be lower, with a maximum of 690 ± 70 and an average of 580 ± 120. Nevertheless, interference from end facet emission was observed (Fig. 4*A*, *Inset*), indicating effective waveguiding and coherent emission from the nanowire. Halide alloying may be pursued in the future to achieve broad wavelength tunability as observed in $CsPbX_3$ quantum dots and $CH_3NH_3PbX_3$ materials (20, 41). In addition to nanowires, well-faceted $CsPbBr_3$ nanoplates were found to lase at ~38 μJ cm^{-2} with the power-dependent emission spectra shown in Fig. 4*B*. Despite the high mode density, peak fitting yields a mode spacing of 3.9 ± 0.7 meV (Fig. S10), which for a 19.3-μm-long plate falls within error of the fit line shown in Fig. 3*E* (*Inset*). This suggests Fabry–Pérot lasing from multiple transverse modes, which may be easily supported by the broad, rectangular plate. This assignment is further supported by the stronger emission intensity observed at one pair of end facets indicating a preference for lasing in that direction (Fig. 4*B*, *Inset*). This lasing behavior is in contrast to whispering gallery mode lasing observed in 100-μm-sized plates of $CsPbBr_3$, which demonstrated broad peak spacing and a uniform spatial emission profile (31).

Here we have reported, to our knowledge, the first successful demonstration of lasing in cesium lead halide nanowires. A facile synthetic procedure was optimized to yield a range of $CsPbBr_3$ nanowires and nanoplates, both of which were found to lase. $CsPbBr_3$ nanowires exhibited low lasing thresholds and relatively high Q factors compared with the field. Most strikingly, the nanowires were stable under both ambient conditions as well as during continuous lasing, important benchmarks for application. Wavelength tunability was also demonstrated through halide substitution, and our ongoing study of anionic alloying indicates the possibility of even greater wavelength tunability across the entire visible spectral range. Overall, we have shown that cesium lead halide nanowires are versatile, stable platforms for future nanophotonic exploration and development.

Materials and Methods

Additional details regarding the materials and methods may be found in the *Supporting Information*.

Synthesis of $CsPbX_3$ Nanowires and Nanoplates. All of the chemicals were purchased from Sigma-Aldrich and used as received unless otherwise stated. Poly(3,4-ethylenedioxythiophene) polystyrene sulfonate (PEDOT:PSS)-coated glass substrates were prepared by cutting ~1 × 1-cm glass substrates and washing sequentially with acetone, isopropanol, and deionized water. Cleaned substrates were then O_2-plasma-treated for 10 min, followed by spin coating with PEDOT:PSS (Solarmer) at 3,000 rpm for 30 s. Afterward, the coated substrates were annealed at 150 °C for 15 min.

To grow CsPbX3 nanowires and nanoplates, 460 mg PbI_2 (99.999%) was dissolved in 1 mL anhydrous dimethylformamide and stirred at 70 °C overnight before further use. The PbI_2 solution was spun onto the PEDOT:PSS-coated glass substrates at 1,000 rpm for 120 s, then annealed at 100 °C for 15 min. The PbI_2 film was carefully submerged into a glass vial with 8 mg/mL CsBr (99.999%) solution in methanol (anhydrous, 99.8%), with the PbI_2 side facing up. The capped reaction vial was heated at 50 °C for 12 h, and the substrate was removed and washed in anhydrous isopropanol for 30 s. The

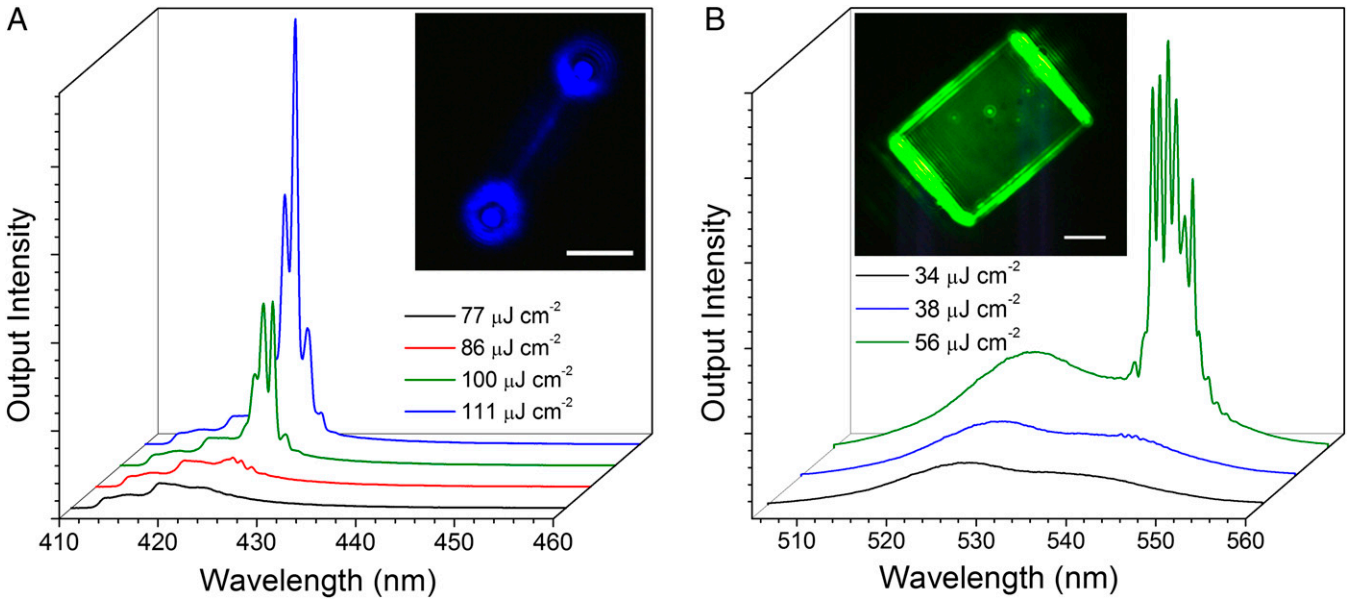

Fig. 4. Lasing in $CsPbCl_3$ nanowires and $CsPbBr_3$ nanoplates. (*A*) $CsPbCl_3$ nanowire power-dependent emission spectra showing lasing at ~425 nm. (*Inset*) Optical image of the same nanowire above the lasing threshold. (Scale bar, 5 μm.) (*B*) $CsPbBr_3$ nanoplate power-dependent emission spectra showing lasing at ~545 nm. (*Inset*) Optical image of the same nanoplate above the lasing threshold. (Scale bar, 5 μm.)

sample was then dried by heating to 50 °C for 5 min. For the synthesis of $CsPbCl_3$ nanowires, the CsBr–methanol solution was replaced with a 6 mg/mL CsCl–methanol solution. The entire growth process was carried out in a nitrogen-filled glove box.

SEM measurements. SEM images were obtained using a JEOL JSM-6340F field-emission SEM. To acquire SEM images of nanowires on fused silica, the substrates were sputter coated with 5-nm gold using a Denton Vacuum Desk IV sputtering system.

XRD measurements. Powder XRD was measured using a Bruker AXS D8 Advance diffractometer with a Cu K_α source.

Transmission electron microscopy and SAED measurements. Characterization of the nanowires by electron diffraction and low-resolution transmission electron microscopy (TEM) was conducted using an FEI Tecnai TEM operating at an accelerating voltage of 200 kV.

PL and TRPL measurements. Individual wires were transferred to fused silica coverslips and secured in N_2-gas-filled cells for all optical measurements, unless otherwise noted. The cells were mounted in a modified Olympus IX71 inverted confocal microscope, equipped with a 2D piezoelectric scanning stage. The second harmonic of the output of a Coherent RegA amplifier (800 nm, 150–200 fs, 295 kHz) seeded by a Coherent Mira oscillator was used as the 400 ± 3-nm excitation light. The 400-nm light was focused to a spot size of 29 ± 4 μm to uniformly illuminate single nanowires using a 50× 0.50-N.A. air objective (Olympus LMPLFLN). Emission from the wires was collected in an epifluorescence scheme; optical wide-field images were taken with an AxioCam MRc5 CCD, while spectra were acquired with a fiber coupled UV-vis spectrometer (Acton Spectra Pro-300i, 1,200 mm^{-1}, 300-nm blaze) equipped with a liquid-N_2-cooled CCD (Roper Scientific 7346–0001). The spectral resolution was 0.06 nm. Lifetime measurements were performed using two avalanche photodiodes (Micro Photon Devices PDM-50 series) input to a time-correlated single-photon counting module (PicoQuant PicoHarp 300/PHR 800) with an instrument response of ∼30 ps. All lasing experiments were conducted at room temperature (26 °C).

ACKNOWLEDGMENTS. This work was supported by the US Department of Energy (DOE) under Contract DE-AC02-05CH11231 (PChem KC3103). Transmission electron microscopy (TEM) characterization was carried out at the National Center for Electron Microscopy and Molecular Foundry. Work at the Molecular Foundry was supported by the Office of Science, Office of Basic Energy Sciences, of the DOE under Contract DE-AC02-05CH11231. S.W.E. thanks the Camille and Henry Dreyfus Foundation for funding, Award EP-14-151. M.L. thanks Suzhou Industrial Park for the fellowship support. J.M. and L.-W.W. thank the support of the Joint Center for Artificial Photosynthesis funded by DOE (DE-SC0004993).

1. Beausoleil RG, Kuekes PJ, Snider GS, Shih-Yuan W, Williams RS (2008) Nanoelectronic and nanophotonic interconnect. *Proc IEEE* 96(2):230–247.
2. Miller DAB (2009) Device requirements for optical interconnects to silicon chips. *Proc IEEE* 97(7):1166–1185.
3. Yan R, et al. (2012) Nanowire-based single-cell endoscopy. *Nat Nanotechnol* 7(3): 191–196.
4. Nakayama Y, et al. (2007) Tunable nanowire nonlinear optical probe. *Nature* 447(7148):1098–1101.
5. Pan L, Bogy DB (2009) Data storage: Heat-assisted magnetic recording. *Nat Photonics* 3(4):189–190.
6. Huang MH, et al. (2001) Room-temperature ultraviolet nanowire nanolasers. *Science* 292(5523):1897–1899.
7. Chu S, et al. (2011) Electrically pumped waveguide lasing from ZnO nanowires. *Nat Nanotechnol* 6(8):506–510.
8. Li KH, Liu X, Wang Q, Zhao S, Mi Z (2015) Ultralow-threshold electrically injected AlGaN nanowire ultraviolet lasers on Si operating at low temperature. *Nat Nanotechnol* 10(2):140–144.
9. Li KH, Liu X, Wang Q, Zhao S, Mi Z (2015) An electrically injected AlGaN nanowire laser operating in the ultraviolet-C band. *Appl Phys Lett* 107(4):043101.
10. Ding K, et al. (2013) Record performance of electrical injection sub-wavelength metallic-cavity semiconductor lasers at room temperature. *Opt Express* 21(4): 4728–4733.
11. Couteau C, Larrue A, Wilhelm C, Soci C (2015) Nanowire lasers. *Nanophotonics* 4(1): 90–107.
12. Eperon GE, Burlakov VM, Docampo P, Goriely A, Snaith HJ (2014) Morphological control for high performance, solution-processed planar heterojunction perovskite solar cells. *Adv Funct Mater* 24(1):151–157.
13. Jeon NJ, et al. (2014) Solvent engineering for high-performance inorganic-organic hybrid perovskite solar cells. *Nat Mater* 13(9):897–903.
14. Liu D, Kelly TL (2014) Perovskite solar cells with a planar heterojunction structure prepared using room-temperature solution processing techniques. *Nat Photonics* 8(2): 133–138.
15. Zhou H, et al. (2014) Interface engineering of highly efficient perovskite solar cells. *Science* 345(6196):542–546.
16. Tan Z-K, et al. (2014) Bright light-emitting diodes based on organometal halide perovskite. *Nat Nanotechnol* 9(9):687–692.
17. Kim Y-H, et al. (2015) Multicolored organic/inorganic hybrid perovskite light-emitting diodes. *Adv Mater* 27(7):1248–1254.
18. Dou L, et al. (2014) Solution-processed hybrid perovskite photodetectors with high detectivity. *Nat Commun* 5:5404.
19. Lin Q, Armin A, Lyons DM, Burn PL, Meredith P (2015) Low noise, IR-blind organohalide perovskite photodiodes for visible light detection and imaging. *Adv Mater* 27(12):2060–2064.
20. Zhu H, et al. (2015) Lead halide perovskite nanowire lasers with low lasing thresholds and high quality factors. *Nat Mater* 14(6):636–642.
21. Xing J, et al. (2015) Vapor phase synthesis of organometal halide perovskite nanowires for tunable room-temperature nanolasers. *Nano Lett* 15(7):4571–4577.
22. Zhang Q, Ha ST, Liu X, Sum TC, Xiong Q (2014) Room-temperature near-infrared high-Q perovskite whispering-gallery planar nanolasers. *Nano Lett* 14(10):5995–6001.
23. Niu G, Guo X, Wang L (2015) Review of recent progress in chemical stability of perovskite solar cells. *J Mater Chem A Mater Energy Sustain* 3(17):8970–8980.
24. Conings B, et al. (2015) Intrinsic thermal instability of methylammonium lead trihalide perovskite. *Adv Energy Mater* 5(15):1500477.
25. Lee J-W, et al. (2015) Formamidinium and cesium hybridization for photo- and moisture-stable perovskite solar cell. *Adv Energy Mater* 5(20):1501310.
26. Stoumpos CC, et al. (2013) Crystal growth of the perovskite semiconductor $CsPbBr_3$: A new material for high-energy radiation detection. *Cryst Growth Des* 13(7):2722–2727.
27. Kulbak M, Cahen D, Hodes G (2015) How important is the organic part of lead halide perovskite photovoltaic cells? Efficient $CsPbBr_3$ cells. *J Phys Chem Lett* 6(13): 2452–2456.
28. Somma F, Nikl M, Nitsch K, Fabeni P, Pazzi GP (2001) Excitons in $CsPbX_3$ (X=Cl, Br, I) ternary nanocrystallites in thin film matrices. *J Lumin* 94–95(0):169–172.
29. Kondo S, Saito T, Asada H, Nakagawa H (2007) Stimulated emission from microcrystalline $CsPbBr_3$ films: Edge emission versus surface emission. *Mater Sci Eng B* 137(1–3): 156–161.
30. Kondo S, et al. (2007) High intensity photoluminescence of microcrystalline $CsPbBr_3$ films: Evidence for enhanced stimulated emission at room temperature. *Curr Appl Phys* 7(1):1–5.
31. Yakunin S, et al. (2015) Low-threshold amplified spontaneous emission and lasing from colloidal nanocrystals of caesium lead halide perovskites. *Nat Commun* 6:8056.
32. Protesescu L, et al. (2015) Nanocrystals of cesium lead halide perovskites ($CsPbX_3$, X = Cl, Br, and I): Novel optoelectronic materials showing bright emission with wide color gamut. *Nano Lett* 15(6):3692–3696.
33. Wang Y, et al. (2015) All-inorganic colloidal perovskite quantum dots: A new class of lasing materials with favorable characteristics. *Adv Mater* 27(44):7101–7108.
34. Zhang D, Eaton SW, Yu Y, Dou L, Yang P (2015) Solution-phase synthesis of cesium lead halide perovskite nanowires. *J Am Chem Soc* 137(29):9230–9233.
35. Ma Y, Guo X, Wu X, Dai L, Tong L (2013) Semiconductor nanowire lasers. *Adv Opt Photonics* 5(3):216–273.
36. Zimmler MA, Bao J, Capasso F, Müller S, Ronning C (2008) Laser action in nanowires: Observation of the transition from amplified spontaneous emission to laser oscillation. *Appl Phys Lett* 93(5):051101.
37. Klimov VI (2007) Spectral and dynamical properties of multiexcitons in semiconductor nanocrystals. *Annu Rev Phys Chem* 58(1):635–673.
38. Johnson JC, Yan H, Yang P, Saykally RJ (2003) Optical cavity effects in ZnO nanowire lasers and waveguides. *J Phys Chem B* 107(34):8816–8828.
39. Johnson JC, et al. (2002) Single gallium nitride nanowire lasers. *Nat Mater* 1(2): 106–110.
40. Sutherland BR, Hoogland S, Adachi MM, Wong CTO, Sargent EH (2014) Conformal organohalide perovskites enable lasing on spherical resonators. *ACS Nano* 8(10): 10947–10952.
41. Nedelcu G, et al. (2015) Fast anion-exchange in highly luminescent nanocrystals of cesium lead halide perovskites ($CsPbX_3$, X = Cl, Br, I). *Nano Lett* 15(8):5635–5640.
42. Kohn W, Sham LJ (1965) Self-consistent equations including exchange and correlation effects. *Phys Rev* 140(4A):A1133–A1138.
43. Perdew JP, Burke K, Ernzerhof M (1996) Generalized gradient approximation made simple. *Phys Rev Lett* 77(18):3865–3868.
44. Kresse G, Furthmüller J (1996) Efficiency of ab-initio total energy calculations for metals and semiconductors using a plane-wave basis set. *Comput Mater Sci* 6(1): 15–50.
45. Kresse G, Joubert D (1999) From ultrasoft pseudopotentials to the projector augmented-wave method. *Phys Rev B: Condens Matter* 59(3):1758–1775.
46. Fox M (2001) *Introduction. Optical Properties of Solids* (Oxford Univ Press, New York), pp 1–20.
47. Malitson IH (1965) Interspecimen comparison of the refractive index of fused silica. *J Opt Soc Am* 55(10):1205–1209.